Supplemental Material

Lead-free room-temperature ferroelectric thermal conductivity switch using anisotropies in thermal conductivities

Lucile Féger[1], Carlos Escorihuela-Sayalero[2], Jean-Michel Rampnoux[3], Kyriaki Kontou[4], Micka Bah[1], Jorge Íñiguez-González[5,6], Claudio Cazorla[2], Isabelle Monot-Laffez[1], Sarah Douri[4,7], Stéphane Grauby[3], Riccardo Rurali[8] ****, Stefan Dilhaire[3] ***, Séverine Gomès[4] **, Guillaume F. Nataf[1] *

[1] GREMAN UMR7347, CNRS, University of Tours, INSA Centre Val de Loire, 37000 Tours, France
[2] Departament de Física, Universitat Politècnica de Catalunya, Campus Nord B4-B5, Barcelona 08034, Spain
[3] Université de Bordeaux, CNRS, LOMA, UMR 5798, F-33400 Talence, France
[4] Univ Lyon, CNRS, INSA-Lyon, Université Claude Bernard Lyon 1, CETHIL UMR5008, F-69621, Villeurbanne, France
[5] Materials Research and Technology Department, Luxembourg Institute of Science and Technology (LIST), L-4362 Esch-sur-Alzette, Luxembourg
[6] Department of Physics and Materials Science, University of Luxembourg, L-4422 Belvaux, Luxembourg
[7] Laboratoire National de Métrologie et d'Essais (LNE), 29, Avenue Roger Hennequin, 78197 Trappes, France
[8] Institut de Ciència de Materials de Barcelona, ICMAB-CSIC, Campus UAB, 08193 Bellaterra, Spain

* guillaume.nataf@univ-tours.fr
** severine.gomes@insa-lyon.fr
*** stefan.dilhaire@u-bordeaux.fr
**** rrurali@icmab.es

SI-I – Frequency-domain thermoreflectance (FDTR)

SI-I.1 TR Frequency range optimization

In FDTR measurements, the lateral thermal resolution is equal to the thermal diffusion length evaluated by $\delta = \sqrt{D/\pi f}$ with D the thermal diffusivity of the material and f the laser modulation frequency [1,2]. Therefore, to simplify the thermal model with a symmetry axis normal to the surface, we adjust the lower frequency of the measured frequency range and the size of both pump and probe beams in such a way as to probe a single domain as shown in Figure SI1. The thermal diffusion length is typically 500 nm at 5 MHz for $BaTiO_3$ and the pump and probe beam diameters are around 12 µm.

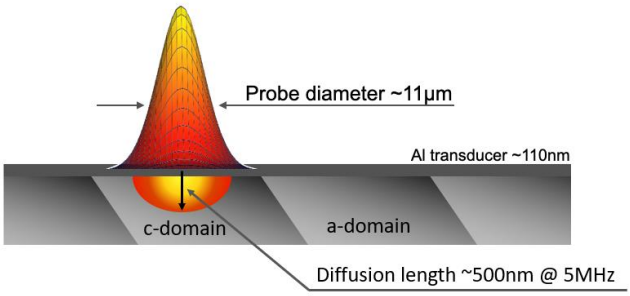

Fig. SI1 Sample cross section with a 110 nm thick Al film on top. *a*-domains and *c*-domains are represented with different gradations of grey. The gaussian shape shows the beam profile focused on the surface of the Al film with a beam size of 11 µm. The gradation in the *c*-domain indicates the probed zone delimited by the diffusion length.

The thermal model then combines the Al layer on top of a single $BaTiO_3$ domain, both separated by a thermal resistance. A comparison between *a*-domain and *c*-domain measured phases and their fits in two adjacent domains is presented in Figure SI2. A good contrast appears for frequencies above 5 MHz. Consequently, the acquisition and optimization will be performed for all measurements in the [5-100 MHz] frequency range. From the phase signal, the inverse problem is solved to identify the thermal conductivity ratio between two adjacent domains.

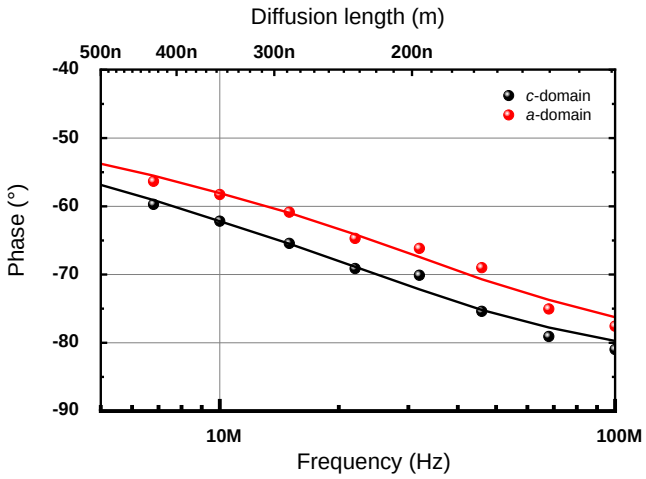

Fig. SI2 Measured thermoreflectance phase signals (dots) for two adjacent domains. The associated best fits are the solid lines. Let us note in addition that, with the combination of the volumetric heat capacity of $BaTiO_3$ (2.64 MJ m^{-3} K^{-1}) and the higher estimated limit of the thermal conductivity (10 W m^{-1} K^{-1}), the thermal penetration depth is around 500 nm at 5 MHz. This is consistent with the needed lateral resolution for the sample geometry and beam sizes.

SI-I.2 Sensitivity analysis: thermal conductivity ratio

A sensitivity analysis of the model parameters shows a very weak sensitivity to the in-plane thermal conductivity of $BaTiO_3$ (cyan curve) in the optimization frequency range (Fig. SI3). This is the reason why the optimization only provides the cross-plane thermal conductivities (black curve). The thermal resistance is nevertheless identifiable (green curves).

Conversely, the model is dependent on the aluminum thickness (blue curve) and the material volumetric heat capacity (purple curve), which is, as expected in this frequency range, completely correlated to the cross-plane thermal conductivity (black curve). However, these data are determined from AFM measurements for the thickness and taken from the literature for the volumetric heat capacity and serve as inputs to the model. Moreover, for the two domain types, these input parameter sensitivities are almost identical. Consequently, for a potential error on these parameters, the variation of the identified thermal conductivity ratio will be weak.

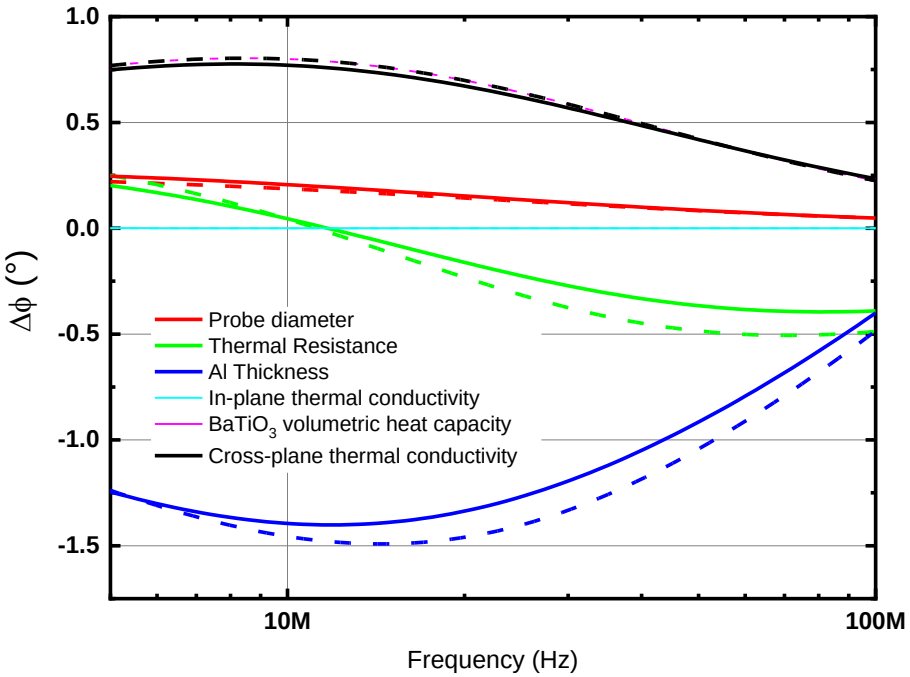

Fig. SI3 For several parameters, sensitivities of $\Delta\phi\,(f)$ defined as the difference of the simulated phases for a 10% parameter variation. The solid (respectively dashed) lines represent the *c*-domains (respectively *a*-domains) sensitivities. Please note that the $BaTiO_3$ volumetric heat capacity sensitivity is overlapped with the $BaTiO_3$ cross-plane thermal conductivity.

In order to demonstrate the reliability of the identified ratio, a parametric analysis of the optimization results was performed on the aluminum thickness and the $BaTiO_3$ volumetric heat capacity. For that purpose, we varied the aluminum thickness from 50 to 150 nm and the volumetric heat capacity of the layer of interest from 2.1 to 3.3 MJ m^{-3} K^{-1}. Based on our set of 6 measurements on the *a*- and *c*-domains, Fig. SI4 shows, for a 2.64 MJ m^{-3} K^{-1} $BaTiO_3$ volumetric heat capacity, the dependence of the identified thermal conductivities on the transducer thickness as expected with the sensitivity curves. However, in the inset, the identified thermal conductivity ratio is almost constant despite of the examined input parameter variations. In addition, the thickness of this curve indicates the volumetric heat capacity change from 2.1 to 3.3 MJ m^{-3} K^{-1}. The thinness of the line shows that this parameter has little influence.

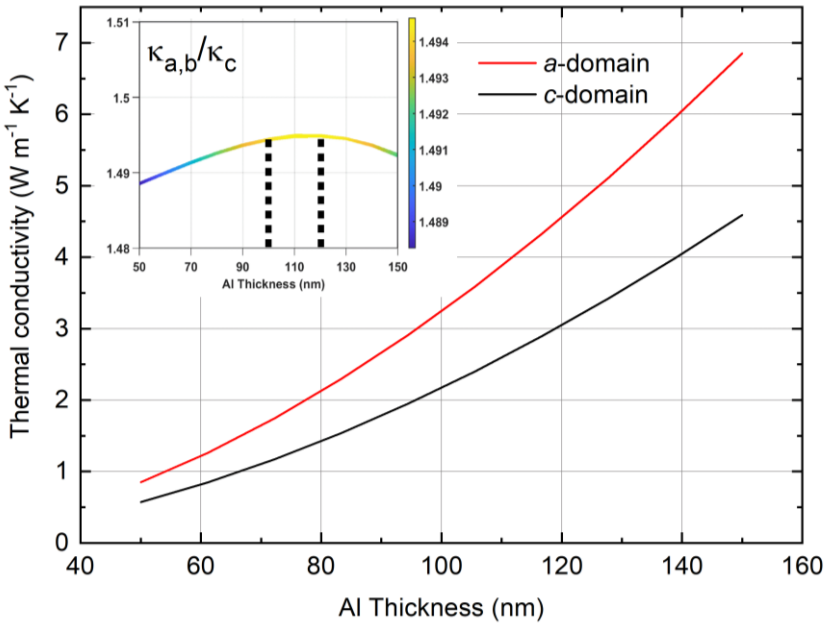

Fig. SI4 Identified thermal conductivity of the *a*-domain and *c*-domain regions as a function of the Al transducer thickness ($BaTiO_3$ volumetric heat capacity is fixed at 2.64 MJ m^{-3} K^{-1}). The inset represents the thermal conductivity ratio $\kappa_{a,b}/\kappa_c$ where the Al thickness is varied from 50 to 150 nm. The varying thickness of the curve is representative of the volumetric heat capacity variation (from 2.1 to 3.3 MJ m^{-3} K^{-1}). The estimated Al thickness values are bounded with the vertical dashed black lines.

SI-II – Scanning thermal microscopy (SThM)

A resistive SThM probe with a palladium (Pd) sensor was used in this work. In SThM measurements, its electrical resistance R is measured by means of a home-made unbalanced Wheatstone bridge powered with a constant current I_w. Values of R and of the electrical current through the probe I can therefore be deduced from the bridge voltage variations ΔV_{out} as the Wheatstone bridge used is symmetrical, $I \cong I_w/2$. Several calibration and modeling steps are needed for deducing, from an R measurement, the thermal conductances and temperatures that are involved in the probe-sample system (Figure SI5). Main calibration steps are given in the following but more details on calibration steps can be found in ref. [3,4].

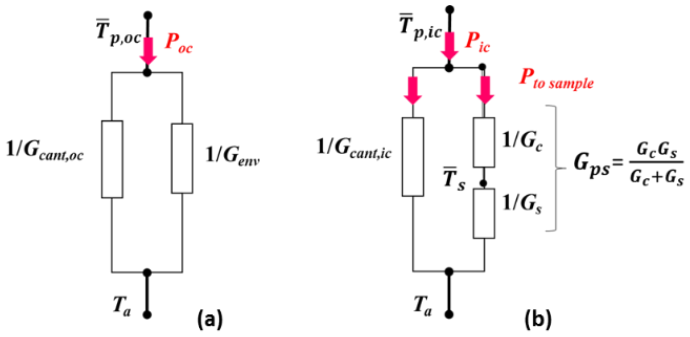

Fig. SI5 Thermal conductance network of the probe-sample system when the probe is not in contact with the sample in air (a) and in contact with a sample (b). Note that the heat transferred from the probe to the environment by thermal radiation and the conducto-convective mechanisms is assumed to be small enough to be neglected when the probe contacts the sample (b). In these Figures, $\overline{T}_{p,oc}$ and $\overline{T}_{p,ic}$, are the mean temperature of the probe out of contact (index *oc*) and in contact (index *ic*) with the sample respectively. P is the power generated by Joule effect in the sensor. $\overline{T}_s$ is the sample surface temperature at the probe-sample thermal contact, averaged on the area of this contact. T_a is ambient temperature. G_{env}, G_{cant}, G_c, G_s and G_{ps} is the thermal conductance associated with the power amount transferred from the hot sensor to its environment, the thermal conductance associated with heat amount transferred from the hot sensor to the cantilever, $P_{to\ cantilever}$, that of the thermal contact, that of the sample and that associated with the heat amount transferred from the hot sensor to the sample through the thermal contact $P_{to\ sample}$.

SI-II.1 SThM probe calibration

SI-II.1.1 Sensor temperature [3,4]

The overall temperature coefficient electrical resistance of the probe $\alpha = (1/R).dR/dT$ was measured as 0.69×10^{-3} K^{-1} from R measurements in an oven as a function of temperature T. In this calibration step, an electrical current of 10 µA was used to minimize Joule heating of the sensor. Knowing α of Pd (α_{Pd} =1.33×10^{-3} K^{-1}**)** and that of the materials of the other metallic components of the probe, the variation of the electrical resistance R_p of the Pd sensor can be estimated as a function of its mean temperature $\overline{T}_{p,oc}$ [3,5]:

$$\Delta R_p = R_p - R_{p0} = R_{p0}\,\alpha_{Pd}\left(\overline{T}_{p,oc} - T_a\right) \quad \text{(SI1)}$$

with R_{p0} = 80.1 Ω the electrical resistance of the Pd wire at ambient temperature T_a (24.7 °C).

SI.II.1.2 Sensor calibration for thermal conductivity measurement [3,4]

In these works, SThM measurements of samples were made from R_p measurements with a probe out of contact (*oc* index) and in contact (*ic* index). They were performed with an electrical current I_w= 2 mA, i.e., using the Pd sensor heated with an electric current I≅1 mA and a sensor temperature measured using Eq. (SI1) to be $\bar{T}_{p,oc}$= 324.8 K, under ambient air conditions, and are based on the estimation of the variation of the probe thermal conductance ΔG_p defined as follows:

$$\Delta G_p = \frac{R_{p,ic} I_{ic}^2}{\bar{T}_{p,ic} - T_a} - \frac{R_{p,oc} I_{oc}^2}{\bar{T}_{p,oc} - T_a} \quad \text{(SI2)}$$

A typical fitting calibration curve $\Delta G_p(k)$ was used to reproduce the variation of in contact measurement of samples with a known thermal conductivity k [3,4]. As the spring constant of the probe used was measured as 0.15 ± 0.02 N.m^{-1} using the reference lever technique, the force between the probe and the sample for contact measurements is estimated as 100 nN.

SI.II.1.3 Sample thermal conductance profile

$BaTiO_3$ sample was measured in imaging mode in the same experimental conditions as the sensor calibration (I≅1 mA, tip-sample force at 100 nN, $\bar{T}_{p,oc}$= 324.8 K and T_a = 24.7 °C). Particular attention was paid to the acquisition time of each image pixel so that it corresponds to about 5 times the probe thermal response time (few ms). Two signals were obtained simultaneously as a function of the probe location (*x*, *y*) on the surface of the sample: the topography signal and the voltage variation ΔV_{out}. In a first approximation, to analyze these measurements, $BaTiO_3$ was taken as a homogeneous material with an isotropic thermal conductivity k_{eff}. Using the calibration curve for thermal conductivity measurement, the k_{eff} profile for the $BaTiO_3$ sample was determined from the ΔV_{out} profiles gained from SThM images. The values determined of $k_{eff,a}$ for in-plane *a*-domains and $k_{eff,c}$ for out-of-plane *c*-domains are 3.9 ± 0.2 W m^{-1} K^{-1} and 3.2 ± 0.2 W m^{-1} K^{-1} respectively. The roughness of the investigated $BaTiO_3$ surface obtained by AFM is lower than 1 nm, so no roughness impact on our measurements has to be taken into account [6].

Based on these k_{eff} values, the local thermal conductance of the sample G_s was found using: $G_s = 4 b_{eff} k_{eff}$ with b_{eff} the effective radius of the thermal contact between the tip and the sample, which is assumed discoidal. Applying this G_s expression supposes b_{eff} larger than the mean free path of phonons (MFP) in the sample. This is the case in this study as b_{eff} has been estimated to be larger than 350 nm (see the following) while the averaged MFP in $BaTiO_3$ is about 100 nm [7,8]. b_{eff} was identified for the two domains of the sample as 385 ± 15 nm using ref. [5]. G_s = 5.6 ± 0.1 µW K^{-1} for *a*-domains and G_s = 5.0 ± 0.1 µW K^{-1} for *c*-domains as reported in the manuscript.

SI-II.2 Components $k_a = k_b$ and k_c identification

Based on k_{eff} values, components $k_a = k_b$ and k_c can also be identified, provided that the temperature at the surface of the sample $T_{s,exp}$ at the probe tip location is known (see Figure SI5(b)). We have considered in this work $T_{s,exp}$ to be the sample surface temperature averaged over the area of effective thermal contact between the tip and the sample. The thermal contact is assumed discoidal, with a radius equal to b_{eff}.

SI-II.2.1 Sample surface temperature $T_{s,exp}$

$T_{s,exp}$ can be estimated applying (Figure SI5b):

$$T_{s,exp} = \bar{T}_{p,ic} - \frac{P_{to\ sample}}{G_c} \quad \text{(SI3)}$$

where G_c is the thermal conductance of the thermal contact and $P_{to\ sample}$ is the heat amount transferred from the hot tip to the sample:

$$P_{to\ sample} = P_{ic} - G_{cant}\,(\bar{T}_{p,ic} - T_a) \quad \text{(SI4)}$$

where G_{cant} is the thermal conductance of the probe determined in vacuum conditions [3].
In Eqs. (SI3) and (SI4), $P_{ic} = R_{p,ic} I_{ic}^2$ and $\bar{T}_{p,ic}$ can be obtained from the value of ΔV_{out} measured on the sample using Eq. (SI1). G_c was calculated knowing that the thermal conductance associated with the heat amount transferred from the hot sensor to the sample can be written as:

$$G_{ps} = \Delta G_p + G_{env} = \frac{G_c}{1+\frac{G_c}{G_s}} \quad \text{(SI5)}$$

where G_{env}, which is the thermal conductance associated to the heat losses to the environment of the probe out of contact with the sample, is determined as in reference [3].

Since the values of k_{eff} and G_s are known for each ferroelectric domain of the sample ($k_{eff,a}$ and $k_{eff,c}$) (see Section SI.II.1.3), G_c can be determined using Eq. (SI5), allowing the estimation of $P_{to\ sample}$ and $T_{s,exp}$ using Eqs. (SI3) and (SI4).

SI-II.2.2 3D numerical model of the sample

We used finite elements modeling based on COMSOL Multiphysics® to establish a three-dimensional model of the thermal transport within the sample. The "Thermal" module of COMSOL® in a static solver configuration was used. In this model, each ferroelectric domain is described by a 500 x 500 x 500 µm^3 parallelepiped block of material with an anisotropic thermal conductivity characterized by components k_x, k_y and k_z in the X, Y and Z directions respectively (Figure SI6).

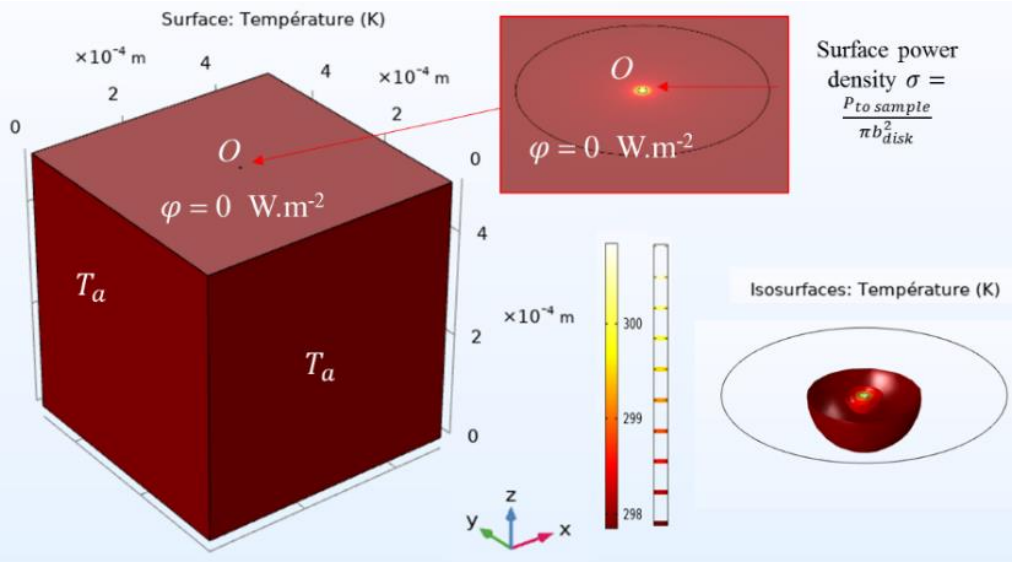

Fig. SI6 3D geometry and boundary conditions for a single domain of the sample.

Depending on domain, $k_y = k_x$ or $k_y = k_z$. The side and bottom faces of the block are at room temperature T_a. Boundary conditions at the top face of the sample (at $z = 500$ µm) are heat deposition on a disk of radius $b_{disk} = b_{eff}$ and centered in O at the middle of the block upper surface with surface power density $\sigma = P_{to\ sample}/\pi b_{disk}^2$ ($r \leq b_{disk}$) and zero heat flux elsewhere.

SI-II.2.3 Methodology for $k_a = k_b$ and k_c identification

The finite elements model has been used to reproduce experimental data in terms of sample surface temperature at the probe location. Model inputs data are b_{eff} and $P_{to\ sample}$ (Eq. (SI4)), which were both derived from experimental measurements (see Sections SI-II.1.3 and SI-II.2. 1), and test values of k_y. Output data is the sample surface temperature at the probe location and averaged on heating source surface area (πb_{disk}^2): $T_{s,mod}$. Components $k_{a,} = k_b$ and k_c are identified when $T_{s,mod} = T_{s,exp}$ for both *c*-domains and *a*-domains simultaneously. In this identification, the least squares approximation method was used.

As shown in Figure SI7, k_c = 2.7 ± 0.4 W m^{-1} K^{-1} and k_a = 4.2 ± 0.3 W m^{-1} K^{-1}. This corresponds to an anisotropy degree of $k_{a,b}/k_c = 1.6 \pm 0.3$.

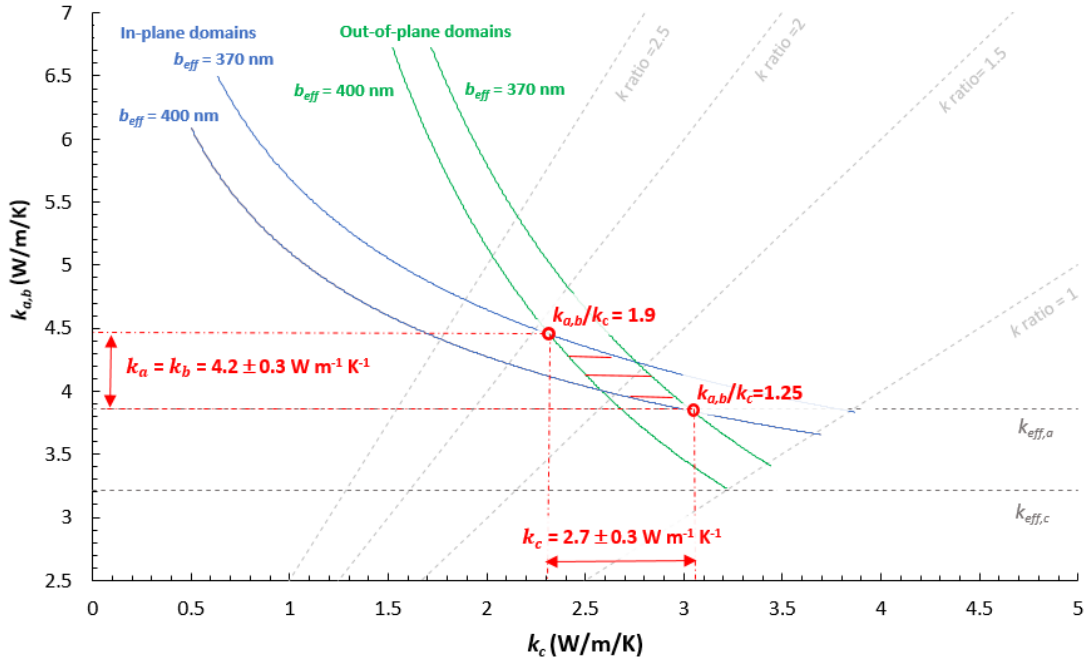

Fig. SI7 Determination of thermal conductivity components and anisotropy degree $k_{a,b}/k_c$ for each domain.

References

[1] Olson, D. H. *et al.* Spatially resolved thermoreflectance techniques for thermal conductivity measurements from the nanoscale to the mesoscale. *Journal of Applied Physics* **126**, 150901 (2019).
[2] Hodges, W. *et al.* Sensing depths in frequency domain thermoreflectance. *Journal of Applied Physics* **131**, 245103 (2022).
[3] Guen, E. *et al.* Scanning thermal microscopy on samples of varying effective thermal conductivities and identical flat surfaces, *J. Appl. Phys.* **128**, 235301 (2020).
[4] Douri, S. *et al.* Numerical investigation of the measurement with a self-heated resistive scanning thermal microscopy probe, submitted in January 2024 to *Measurement Science and Technology*.
[5] Assy, A. *et al.* Heat transfer at nanoscale contacts investigated with scanning thermal microscopy, *Applied Physics Letters*, 109901 (2015).
[6] Guen, E. *et al.* Impact of roughness on heat conduction involving nanocontacts. *Applied Physics Letters*, **119**, no 16 (2021).
[7] Limelette, P. *et al.* Influence of ferroelastic domain walls on thermal conductivity. *Phys. Rev. B* **108**, 144104 (2023).
[8] Negi, A. *et al.* Thickness-Dependent Thermal Conductivity and Phonon Mean Free Path Distribution in Single-Crystalline Barium Titanate. *Adv. Sci.* **2301273**, 1–10 (2023).